Computer Methods and Programs in Biomedicine 226 (2022) 107164

Contents lists available at ScienceDirect

Computer Methods and Programs in Biomedicine

journal homepage: www.elsevier.com/locate/cmpb

A meshless fragile points method for rule-based definition of myocardial fiber orientation

Konstantinos A. Mountris[a,b], Esther Pueyo[a,b,*]

[a] Aragón Institute for Engineering Research, University of Zaragoza, IIS Aragón, Zaragoza, Spain
[b] CIBER in Bioengineering, Biomaterials & Nanomedicine (CIBER-BBN), Spain

ARTICLE INFO

Article history:
Received 5 April 2022
Revised 18 September 2022
Accepted 27 September 2022

Keywords:
Cardiac
Fibers
Meshless
Laplace–Dirichlet
Fragile points method
FPM

ABSTRACT

Background and objective: Rule-based methods are commonly used to estimate the arrangement of myocardial fibers by solving the Laplace problem with appropriate Dirichlet boundary conditions. Existing algorithms are using the Finite Element Method (FEM) to solve the Laplace–Dirichlet problem. However, meshless methods are under development for cardiac electrophysiology simulation. The objective of this work is to propose a meshless rule based method for the determination of myocardial fiber arrangement without requiring a mesh discretization as it is required by FEM.

Methods: The proposed method employs the Fragile Points Method (FPM) for the solution of the Laplace–Dirichlet problem. FPM uses simple discontinuous trial functions and single-point exact integration for linear trial functions that set it as a promising alternative to the Finite Element Method. We derive the FPM formulation of the Laplace–Dirichlet and we estimate ventricular and atrial fiber arrangements according to rules based on histology findings for four different geometries. The obtained fiber arrangements from FPM are compared with the ones obtained from FEM by calculating the angle between the fiber vector fields of the two methods for three different directions (i.e., longitudinal, sheet, transverse).

Results: The fiber arrangements that were generated with FPM were in close agreement with the generated arrangements from FEM for all three directions. The mean angle difference between the FPM and FEM vector fields were lower than 0.030° for the ventricular fiber arrangements and lower than 0.036° for the atrial fiber arrangements.

Discussion: The proposed meshless rule-based method was proven to generate myocardial fiber arrangements with very close agreement with FEM while alleviates the requirement for a mesh of the latter. This is of great value for cardiac electrophysiology solvers that are based on meshless methods since they require a well defined myocardial fiber arrangement to simulate accurately the propagation of electrical signals in the heart. Combining a meshless solution for both the determination of the fibers and the electrical signal propagation can allow for solution that do not require the definition of a mesh. To our knowledge, this work is the first one to propose a meshless rule-based method for myocardial fiber arrangement determination.

1. Introduction

Healthy and diseased heart structure and function is to a good extent determined by the arrangement of myocardial fibers. Under certain disease conditions like hypertrophy and myocardial infarction, changes in the arrangement and alignment of cardiac fibers can be an adaptive mechanism to partially restore the contractile function. However, this restoration may happen at the expense of electrical stability [1]. In silico models aiming to provide insight into such disease mechanisms require proper definition of myocardial fiber arrangement [2,3].

Nowadays, detailed definition of myocardial fibers can be obtained using advanced imaging modalities like diffusion tensor magnetic resonance imaging (DT-MRI) [4,5], micro-computed tomography (micro-CT) [6] or shear wave imaging [7]. These imaging

* Corresponding author at: Aragón Institute for Engineering Research, University of Zaragoza, IIS Aragón, Zaragoza, Spain.
E-mail addresses: kmountris@unizar.es (K.A. Mountris), epueyo@unizar.es (E. Pueyo).

https://doi.org/10.1016/j.cmpb.2022.107164

techniques have proved to be very useful for *ex vivo* determination of myocardial fibers. However, they require long acquisition times that challenge *in vivo* application. Recently, promising DTI-MRI sequences for *in vivo* definition of myocardial fibers have been proposed [8,9]. Nevertheless, these techniques remain limited to coarse spatial resolution. Imaging techniques present even more important limitations when atrial fiber orientation is considered. This is mainly due to the imaging difficulties posed by the thin atrial walls [10]. Only recently, submillimeter DT-MRI techniques made the analysis of *ex vivo* atrial fibers possible [11,12].

An alternative approach for the determination of high-resolution fiber orientation is the use of rule-based methods (RBM). In traditional RBM, minimal distance parametrization has been used to define the transmural and apicobasal directions [13]. However, such parametrizations can suffer from singularities, especially at the septum and endocardium structures (e.g. papillary muscles) [14]. To avoid the singularity problem, modern RBM, known as Laplace–Dirichlet RBM (LDRBM), solve the Laplacian problem with properly defined Dirichlet boundary conditions to define a smooth orthonormal coordinate system [15–17]. Rotation rules based on anatomical observations are then applied on the coordinate system to generate realistic fiber orientation. LDRBM have been developed mainly for fiber determination in ventricular models with a basal clip [15]. Doste et al. have extended this algorithm to account for fiber orientation in the outflow tracts considering complete biventricular models [16]. Recently, a new LDRBM dedicated for atrial fiber orientation has been proposed [17], where the individual fiber bundles of the atria and their dimensions are determined based on the specified rules. The combination of ventricular and atrial LDRBM allows the determination of realistic fiber arrangement of four-chamber heart models that can be used later on for cardiac electrophysiology (EP) simulation.

Commonly, in silico cardiac EP employs the Finite Element Method (FEM) for the solution of either the bidomain [18] or monodomain model [19]. FEM is widely appreciated for its robustness and accuracy. However, it requires the construction of a well-defined mesh. This is a tedious process, especially for structures with complex geometry like the heart. On the other hand, meshless methods alleviate the requirement of a mesh [20,21]. Instead of interconnected elements, the numerical approximation is performed on a cloud of randomly distributed nodes supporting the point of interest (support domain). Due to this property, different meshless methods have been considered as an alternative to FEM for cardiac EP. The element-free Galerkin (EFG) method has been used to solve the monodomain model for the simulation of the electrical activity in the left ventricle [22]. EFG is based on the Galerkin formulation similar to FEM satisfying zero Neumann boundary conditions naturally. However, a special treatment is required for the imposition of Dirichlet boundary conditions due to the use of non-interpolating approximation functions. A remedy to this issue has been proposed with the development of the maximum entropy approximation [23,24], which possesses a weak-Kronecker delta property that allows the direct imposition of Dirichlet boundary conditions. Alternatively, the mixed collocation method (MCM) has been used for the solution of the monodomain model in cardiac EP [25,26]. MCM has the advantage of directly imposing Dirichlet conditions through collocation. However, numerical instability may be introduced at Neumann boundaries and a fine nodal discretization is usually required to avoid this problem [27].

Recently, a new promising meshless method, the Fragile Points Method (FPM), has been introduced [28–32]. FPM is based on the Galerkin weak form like EFG but without its limitations since it uses local, simple, polynomial, discontinuous functions [33] as trial and test functions. Moreover, the integration in the Galerkin weak form is trivial and Dirichlet as well as Neumann boundary conditions can be imposed as in FEM. However, a special treatment is required to treat the inconsistency of the global matrices that arise due to the discontinuity of the trial and test functions. Numerical flux corrections, which are common in Discontinuous Galerkin methods [34], are used in FPM to avoid the inconsistency issue, leading to sparse and symmetric global matrices.

In this work, we employ FPM for the solution of the Laplace problem for the definition of myocardial fiber arrangement. Our motivation is to provide a robust meshless algorithm to compute fiber orientation in meshless models where a mesh topology may not be available. We consider the generation of both ventricular and atrial fiber arrangements using FPM and we compare our results with those obtained by FEM.

2. Methods

2.1. Laplace–Dirichlet problem for fiber generation

Fiber orientation generation using LDRBM requires the solution of the Laplace equation. Appropriate Dirichlet boundary conditions are defined to obtain the transmural and apico-basal directions. The general form of the Laplace problem is given by:

$$\begin{cases} \boldsymbol{\Delta}\chi = 0 & \text{in } \Omega \\ \chi = g_D & \text{in } \Gamma_D \\ \boldsymbol{\nabla}\chi \cdot \boldsymbol{n} = \boldsymbol{g} \cdot \boldsymbol{n} = g_N & \text{in } \Gamma_N \end{cases}, \tag{1}$$

where χ represents either the transmural (Φ) or the apico-basal (Ψ) unknown in the myocardial domain Ω with boundary $\Gamma_D \cup \Gamma_N = \partial\Omega$. g_D, $g_N \in \mathbb{R}$ define the prescribed values of the unknown at the Dirichlet and Neumann boundaries, respectively. For the solution of the Laplace problem in LDRBM, $g_N = 0$ is used.

2.2. Solution to the Laplace–Dirichlet problem through the fragile points method

2.2.1. Construction of trial and test functions

In the Fragile Points Method (FPM), we consider randomly scattered points inside the domain Ω and its boundary $\partial\Omega$ without requiring any connectivity knowledge. We partition Ω into conforming non-overlapping subdomains with each subdomain containing only one point. We employ the simple Voronoi diagram method for the partition of Ω leading to polygonal/polyhedral subdomains in 2D/3D as in Fig. 1. For each subdomain, a simple local discontinuous polynomial trial function is defined in terms of the values of χ and $\frac{\partial\chi}{\partial x}$, $\frac{\partial\chi}{\partial y}$, $\frac{\partial\chi}{\partial z}$ at its internal point. For the subdomain E_0 containing the internal point P_0 of coordinates (x_0, y_0, z_0), the trial function χ_h in E_0 is written as:

$$\chi_h(\boldsymbol{x}) = \chi_0 + \left.\frac{\partial\chi}{\partial x}\right|_{P_0}(x - x_0) + \left.\frac{\partial\chi}{\partial y}\right|_{P_0}(y - y_0) + \left.\frac{\partial\chi}{\partial z}\right|_{P_0}(z - z_0), \quad \boldsymbol{x} = (x, y, z) \in E_0. \tag{2}$$

χ_0 is the value of χ at point P_0 and (x_0, y_0, z_0) denotes the coordinates of P_0. The derivatives $\frac{\partial\chi}{\partial x}$, $\frac{\partial\chi}{\partial y}$, $\frac{\partial\chi}{\partial z}$ at P_0 are unknowns that are computed using the Generalized Finite Difference (GFD) method [33]. To solve for the unknown derivatives, we first define the support domain of P_0 as the nearest points $P_1, P_2, \ldots, P_m$ to P_0, included in E_i, $i = 1, 2, \ldots, m$, respectively, that are attached to E_0. Next, we define the weighted discrete L^2 norm J:

$$J = \sum_{i=1}^{m} \left(\left.\frac{\partial\chi}{\partial x}\right|_{P_0}(x_i - x_0) + \left.\frac{\partial\chi}{\partial y}\right|_{P_0}(y_i - y_0) + \left.\frac{\partial\chi}{\partial z}\right|_{P_0}(z_i - z_0) - (\chi_i - \chi_0) \right)^2 w_i, \tag{3}$$

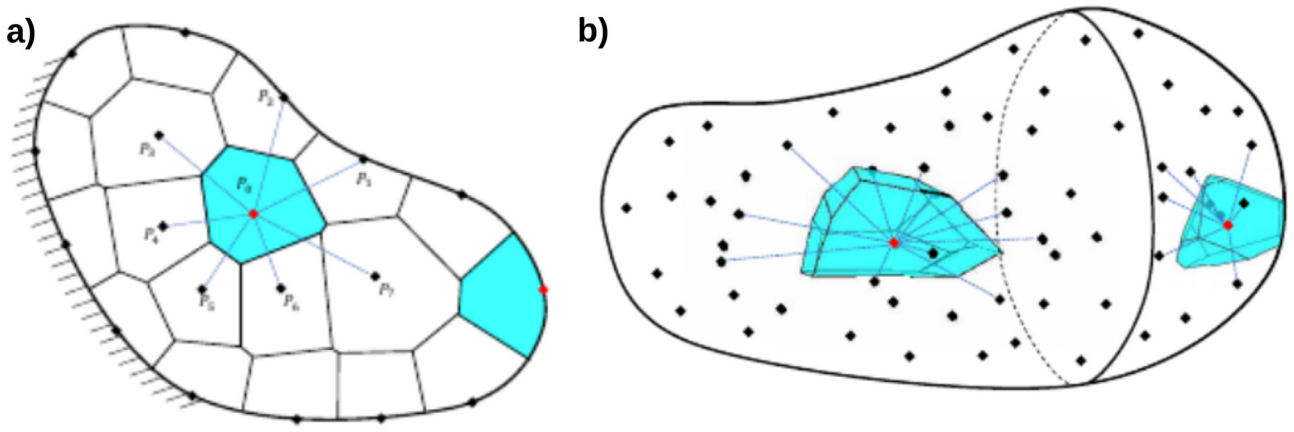

Fig. 1. Non-overlapping subdomains enclosing the meshless discretization of a domain Ω with irregularly distributed points. a) Polygonal subdomains of a 2D domain. b) Polyhedral subdomains of a 3D domain.

where (x_i, y_i, z_i) denotes the coordinate vector of the internal point $P_i \in E_i$, χ_i is the value of χ_h at P_i and w_i is the value of the weight function at P_i, $i = 1, 2, \ldots, m$. Constant weight functions are considered in this work. From the stationarity of J, the gradient of χ at P_0 is obtained by Dong et al. [35]:

$$\nabla\chi\Big|_{P_0} = (\boldsymbol{A}^T\boldsymbol{A})^{-1}\boldsymbol{A}^T(\boldsymbol{\chi}_m - \chi_0\boldsymbol{I}_m), \tag{4}$$

where

$$\boldsymbol{A} = \begin{bmatrix} x_1 - x_0 & y_1 - y_0 & z_1 - z_0 \\ x_2 - x_0 & y_2 - y_0 & z_2 - z_0 \\ & \vdots & \\ x_m - x_0 & y_m - y_0 & z_m - z_0 \end{bmatrix}$$

$$\boldsymbol{\chi}_m = [\chi_1 \quad \chi_2 \quad \ldots \quad \chi_m]^T$$

$$\nabla\chi = \left[\frac{\partial\chi}{\partial x} \quad \frac{\partial\chi}{\partial y} \quad \frac{\partial\chi}{\partial z}\right]^T$$

$$\boldsymbol{I}_m = [1 \quad 1 \quad \ldots \quad 1]^T_{1\times m}.$$

For convenience, Eq. (4) is rewritten in terms of $\boldsymbol{\chi}_E$ as

$$\nabla\chi = \boldsymbol{B}\boldsymbol{\chi}_E \quad \text{at point } P_0, \tag{5}$$

where the matrix $\boldsymbol{B}$ and vector $\boldsymbol{\chi}_E$ are given by:

$$\boldsymbol{B} = (\boldsymbol{A}^T\boldsymbol{A})^{-1}\boldsymbol{A}^T \begin{bmatrix} -1 & 1 & 0 & \ldots & 0 \\ -1 & 0 & 1 & \ddots & \vdots \\ \vdots & \vdots & \ddots & \ddots & 0 \\ -1 & 0 & \ldots & 0 & 1 \end{bmatrix}_{m\times(m+1)}, \tag{6}$$

$$\boldsymbol{\chi}_E = [\chi_0 \quad \chi_1 \quad \chi_2 \quad \ldots \quad \chi_m]^T \tag{7}$$

From the constitution of $\nabla\chi\Big|_{P_0}$, we can express χ_h in Eq. (2) in terms of χ_E:

$$\chi_h(\boldsymbol{x}) = \boldsymbol{N}\boldsymbol{\chi}_E, \quad \forall\boldsymbol{x} \in E_0, \tag{8}$$

where $\boldsymbol{N}$ denotes the shape function of χ_h in E_0:

$$\boldsymbol{N} = [\boldsymbol{x} - \boldsymbol{x}_0]\boldsymbol{B} + \begin{bmatrix} 1 & 0 & \ldots & 0 \end{bmatrix}_{1\times(m+1)}. \tag{9}$$

The matrix $\boldsymbol{N}$ denotes the shape function of χ_h in E_0 in terms of $P_0, P_1, P_2, \ldots, P_m$. The same functions are also used as test functions in the Galerkin weak form.

2.2.2. The Galerkin weak form

The Galerkin weak form of the Laplace problem is obtained by multiplying a test function v on both sides and integrating by parts using Green's identity and the assumption that $v = 0$ on $\partial\Omega$. Omitting the boundary conditions, Eq. (1) in its weak form is given by:

$$\sum\int_{E_i} \nabla\chi \cdot \nabla v d\Omega = 0. \tag{10}$$

By substituting the trial and test functions into Eq. (10), the point stiffness matrix of P_0 can be derived as:

$$K_{E_0} = \int_{E_0} \boldsymbol{B}^T\boldsymbol{B} d\Omega. \tag{11}$$

Since linear interpolation is employed for χ_h and v, $\boldsymbol{B}$ is a constant matrix. Thus, the integral can be computed by multiplying the value of $\boldsymbol{B}^T\boldsymbol{B}$ by the area of E_0:

$$K_{E_0} = \boldsymbol{B}^T\boldsymbol{B}S_{E_0}, \tag{12}$$

where S_{E_0} is the area of E_0. By assembling all the point stiffness matrices, we can obtain the global stiffness matrix of the domain Ω, similarly to FEM but with point stiffness matrices rather than element stiffness matrices. It should be noted here that, due to the discontinuity of the shape functions, the resulting global stiffness matrix is inconsistent. To remedy this issue numerical flux corrections are applied.

2.2.3. Numerical flux corrections for inconsistency

Here we address the inconsistency issue by introducing the numerical flux corrections concept [34]. We first rewrite Eq. (1) using two variables χ and $\boldsymbol{\sigma}$:

$$\begin{cases} \boldsymbol{\sigma} = \nabla\chi & \text{in } \Omega \\ -\nabla\cdot\boldsymbol{\sigma} = 0 & \text{in } \Omega \\ \chi = g_D & \text{in } \Gamma_D \\ \boldsymbol{\sigma}\cdot\boldsymbol{n} = g_N & \text{in } \Gamma_N \end{cases}. \tag{13}$$

The first two equations in Eq. (13) are multiplied by the test functions $\boldsymbol{\tau}$, v and are integrated by parts over E to obtain the weak forms:

$$\int_E \boldsymbol{\sigma}_h \cdot \boldsymbol{\tau} d\Omega = -\int_E \nabla\chi_h \cdot \boldsymbol{\tau} d\Omega + \int_{\partial E} \hat{\chi}_h\boldsymbol{n}\cdot\boldsymbol{\tau} d\Gamma \tag{14}$$

$$\int_E \boldsymbol{\sigma}_h \cdot \nabla v d\Omega = \int_{\partial E} \hat{\boldsymbol{\sigma}}_h \cdot \boldsymbol{n} v d\Gamma, \tag{15}$$

where the numerical solutions χ_h and $\boldsymbol{\sigma}_h$ should satisfy the two above equations for every subdomain E and $\hat{\chi}_h$ and $\hat{\boldsymbol{\sigma}}_h$ are the numerical fluxes that approximate χ_h and $\boldsymbol{\sigma}_h$, respectively, on the

boundary of E. By summing Eqs. (14) and (15) over all the subdomains, as in Dong et al. [35], we obtain:

$$\int_{\Omega} \boldsymbol{\sigma}_h \cdot \boldsymbol{\tau} d\Omega = -\int_{\Omega} \nabla \chi_h \cdot \boldsymbol{\tau} d\Omega + \int_{\Gamma} [\![\hat{\chi}_h]\!] \cdot \{\boldsymbol{\tau}\} d\Gamma + \int_{\Gamma_h} \{\hat{\chi}_h\} [\![\boldsymbol{\tau}]\!] d\Gamma \tag{16}$$

$$\int_{\Omega} \boldsymbol{\sigma}_h \cdot \nabla v d\Omega - \int_{\Gamma} \{\hat{\boldsymbol{\sigma}}_h\} \cdot [\![v]\!] d\Gamma - \int_{\Gamma_h} [\![\hat{\boldsymbol{\sigma}}_h]\!] \{v\} d\Gamma = 0, \tag{17}$$

where Γ is the set of all boundaries and Γ_h denotes the internal boundaries, $\Gamma_h = \Gamma - \Gamma_D - \Gamma_N$. The average operator $\{\}$, and the jump operator $[\![]\!]$ are defined, respectively, as:

$$[\![v]\!] = \begin{cases} v_1 \boldsymbol{n_1} + v_2 \boldsymbol{n_2} & e \in \Gamma_h \\ v \boldsymbol{n} & e \in \partial\Omega \end{cases}, \quad \{v\} = \begin{cases} \frac{1}{2}(v_1 + v_2) & e \in \Gamma_h \\ v & e \in \partial\Omega \end{cases} \tag{18}$$

$$[\![\boldsymbol{\tau}]\!] = \begin{cases} \boldsymbol{\tau}_1 \cdot \boldsymbol{n_1} + \boldsymbol{\tau}_2 \cdot \boldsymbol{n_2} & e \in \Gamma_h \\ \boldsymbol{\tau} \cdot \boldsymbol{n} & e \in \partial\Omega \end{cases}, \quad \{\boldsymbol{\tau}\} = \begin{cases} \frac{1}{2}(\boldsymbol{\tau}_1 + \boldsymbol{\tau}_2) & e \in \Gamma_h \\ \boldsymbol{\tau} & e \in \partial\Omega \end{cases} \tag{19}$$

Where $\boldsymbol{n}_1 = -\boldsymbol{n}_2$ denote the outward normal vectors of the two subdomains that share $e \in \Gamma_h$. Finally, the internal penalty numerical flux is applied on Γ_h with penalty parameter η. Replacing $\boldsymbol{\sigma}_h$ with $\nabla \chi_h$, we obtain the consistent weak form:

$$\begin{aligned} &\sum_{E \in \Omega} \int_E \nabla \chi_h \cdot \nabla v d\Omega - \sum_{e \in \Gamma_h \cup \Gamma_D} \int_e (\{\nabla \chi_h\} [\![v]\!] + \{\nabla v\} [\![\chi_h]\!]) d\Gamma \\ &\quad + \sum_{e \in \Gamma_h \cup \Gamma_D} \frac{\eta}{h_e} \int_e [\![\chi_h]\!] [\![v]\!] d\Gamma \\ &= \sum_{e \in \Gamma_D} \int_e (\frac{\eta}{h_e} v - \nabla v \cdot \boldsymbol{n}) g_D d\Gamma + \sum_{e \in \Gamma_N} \int_e u g_N d\Gamma, \end{aligned} \tag{20}$$

where h_e denotes a boundary-dependent parameter with the unit of length and it is defined as the distance between points i, j when the segment $e \in \partial E_i \cap \partial E_j$. The penalty parameter η, $\eta > 0$, is independent of the boundary size and should be large enough to ensure stability.

Substituting $\boldsymbol{B}$ for $\nabla \chi_h$ and ∇v and N for χ_h and v into Eq. (20), we can write the point stiffness matrix K_E and the boundary stiffness matrices K_h and K_D as:

$$\begin{cases} K_E = \int_E \boldsymbol{B}^T \boldsymbol{B} d\Omega \quad \text{where } E \in \Omega \\ K_h = \frac{-1}{2} \int_e (\boldsymbol{B}_1^T \boldsymbol{n}_1^T \boldsymbol{N}_1 + \boldsymbol{N}_1^T \boldsymbol{n}_1^T \boldsymbol{B}_1) d\Gamma + \frac{\eta}{h_e} \int_e \boldsymbol{N}_1^T \boldsymbol{N}_1 d\Gamma \\ \quad + \frac{-1}{2} \int_e (\boldsymbol{B}_2^T \boldsymbol{n}_2^T \boldsymbol{N}_2 + \boldsymbol{N}_2^T \boldsymbol{n}_2^T \boldsymbol{B}_2) d\Gamma + \frac{\eta}{h_e} \int_e \boldsymbol{N}_2^T \boldsymbol{N}_2 d\Gamma \\ \quad + \frac{-1}{2} \int_e (\boldsymbol{B}_2^T \boldsymbol{n}_1^T \boldsymbol{N}_1 + \boldsymbol{N}_2^T \boldsymbol{n}_2^T \boldsymbol{B}_1) d\Gamma - \frac{\eta}{h_e} \int_e \boldsymbol{N}_1^T \boldsymbol{N}_2 d\Gamma \\ \quad + \frac{-1}{2} \int_e (\boldsymbol{B}_1^T \boldsymbol{n}_2^T \boldsymbol{N}_2 + \boldsymbol{N}_1^T \boldsymbol{n}_1^T \boldsymbol{B}_2) d\Gamma - \frac{\eta}{h_e} \int_e \boldsymbol{N}_2^T \boldsymbol{N}_1 d\Gamma \quad \text{where } e = \partial E_1 \cap \partial E_2 \in \Omega \\ K_D = \frac{-1}{2} \int_e (\boldsymbol{N}^T \boldsymbol{n}^T \boldsymbol{B} + \boldsymbol{B}^T \boldsymbol{n}^T \boldsymbol{N}) d\Gamma + \frac{\eta}{h_e} \int_e \boldsymbol{N}^T \boldsymbol{N} d\Gamma \quad \text{where } e \in \Gamma_D \end{cases} \tag{21}$$

By assembling all the submatrices, we obtain the global stiffness matrix $\boldsymbol{K}$ in a similar manner as in FEM:

$$\boldsymbol{K\chi} = \boldsymbol{0} \tag{22}$$

The resulting stiffness matrix is symmetric, sparse and positive definitive.

2.3. Ventricular fiber arrangement

We consider the generation of ventricular fibers for the general case of a biventricular model with outflow tracts (OT) using the proposed LDRBM by Doste et al. [16]. The Laplace problem is solved by applying Dirichlet boundary conditions at the surfaces of the right ventricle (RV) endocardium, left ventricle (LV) endocardium, biventricular epicardium and cardiac valves (mitral and aortic valves in the LV, pulmonary and tricuspid valves in the RV).

Table 1
Model mesh information.

Model	Nodes	Elements	Dual cells
M1	84,022	299,966	84,022
M2	85,890	303,626	85,890
M3	87,501	307,036	87,501
M4	83,194	291,468	83,194

Table 2
Boundary conditions for generating ventricular fiber orientation.

Type	χ	g_{Da}	Γ_{Da}	g_{Db}	Γ_{Db}
LV	Φ	-2	Γ_{LVendo}	0	Γ_{LVepi}
	Ψ_{a1}	0	Γ_{MV}	1	Γ_{LVapex}
	Ψ_{a2}	0	Γ_{AV}	1	Γ_{LVapex}
	w	1	$\Gamma_{MV} \cup \Gamma_{LVapex}$	0	Γ_{AV}
	s	1	Γ_S	0	Γ_{LVendo}
RV	Φ	1	Γ_{RVendo}	0	Γ_{RVepi}
	Ψ_{a1}	0	Γ_{TV}	1	Γ_{RVapex}
	Ψ_{a2}	0	Γ_{PV}	1	Γ_{RVapex}
	w	1	$\Gamma_{TV} \cup \Gamma_{RVapex}$	0	Γ_{PV}
	s	1	Γ_S	0	Γ_{RVendo}

[Da] First Dirichlet condition.
[Db] Second Dirichlet condition.

Transmural direction ($\nabla\Phi$) is obtained by computing the gradient of the solution to the Laplace problem (Eq. (1)) with Dirichlet boundary conditions applied on LV endocardium (Γ_{LVendo}), RV endocardium (Γ_{RVendo}) and epicardium (Γ_{epi}). By assigning $\Phi = -2$ at Γ_{LVendo} and $\Phi = 1$ at Γ_{RVendo}, we obtain $\Phi < 0$ in LV and $\Phi > 0$ in RV that allows partitioning the volume of the two ventricles. Furthermore, these boundary conditions result in the assignment of two-thirds of the septum to the LV as indicated from histological studies [36,37].

The apicobasal direction ($\nabla\Psi$) is defined individually for each ventricle as the weighted sum of the two gradients originating from the apex towards the base and the outflow tracts of the ventricle and is given by:

$$\nabla\Psi = \nabla\Psi_{a1} \cdot w + \nabla\Psi_{a2} \cdot (1 - w) = 0 \tag{23}$$

where for the case of LV, $\nabla\Psi_{a1}$ and $\nabla\Psi_{a2}$ define the gradients from LV apex (Γ_{LVapex}) to mitral valve (Γ_{MV}) and from Γ_{LVapex} apex to aortic valve (Γ_{AV}), respectively. Similarly, $\nabla\Psi_{a1}$ and $\nabla\Psi_{a2}$ correspond to the gradients from Γ_{RVapex} to tricuspid valve (Γ_{TV}) and from Γ_{RVapex} to pulmonary valve (Γ_{PV}) for the case of RV. The function w denotes the intraventricular interpolation function that is used to define the weights of $\nabla\Psi_{a1}$ and $\nabla\Psi_{a2}$ in the computation of $\nabla\Psi$.

The function w is obtained by solving the Laplace problem with appropriate boundary conditions (see Table 2). Also, it enables controlling the smoothness of fiber changes near the OT by modifying the boundary data. Finally, fiber continuity in the septum (s) is computed by solving the Laplace problem with Dirichlet boundary conditions $s = 1$ assigned at the interventricular septal surface (Γ_S) and $s = 0$ at the LV and RV endocardia. The partition of the ventricles and the definition of the different directions are depicted in Fig. 2.

The local coordinate system ($\hat{\boldsymbol{e}}_l$, $\hat{\boldsymbol{e}}_n$, $\hat{\boldsymbol{e}}_t$) is obtained by the apicobasal and transmural gradients ($\nabla\Psi$, $\nabla\Phi$) with the longitudinal direction ($\hat{\boldsymbol{e}}_l$) along the fiber defined as the cross product of transmural ($\hat{\boldsymbol{e}}_t$) and normal directions ($\hat{\boldsymbol{e}}_n$):

$$\hat{\boldsymbol{e}}_n = \frac{\nabla\Psi}{\|\nabla\Psi\|}, \quad \hat{\boldsymbol{e}}_t = \frac{\nabla\Phi - (\hat{\boldsymbol{e}}_n \cdot \nabla\Phi)\hat{\boldsymbol{e}}_n}{\|\nabla\Phi - (\hat{\boldsymbol{e}}_n \cdot \nabla\Phi)\hat{\boldsymbol{e}}_n\|}, \quad \hat{\boldsymbol{e}}_l = \hat{\boldsymbol{e}}_n \times \hat{\boldsymbol{e}}_t \tag{24}$$

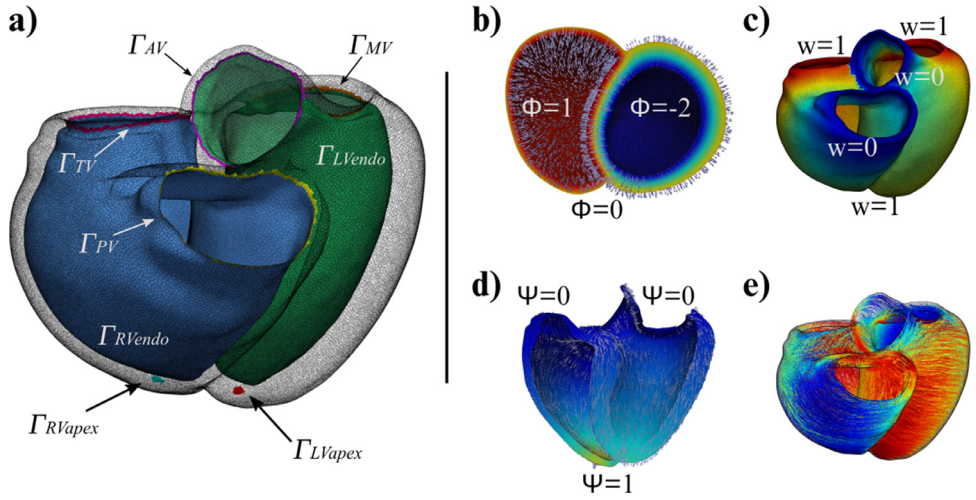

Fig. 2. a) Partition of the ventricular geometry boundary. b) Transmural distance (Φ) and its gradient ($\nabla\Phi$). c) Intraventricular function (w). d) Apicobasal distance (Ψ) and its gradient ($\nabla\Psi$). e) Ventricular fiber arrangement ($\hat{\boldsymbol{e}}_l$).

The final fiber arrangement is determined by applying a counterclockwise rotation to the vector $\hat{\boldsymbol{e}}_l$ around the vector $\hat{\boldsymbol{e}}_t$ by an angle α:

$$\alpha = \alpha_{endo}(w) \cdot (1 - \tilde{\Phi}) + \alpha_{epi}(w) \cdot \tilde{\Phi} \tag{25}$$

where $\tilde{\Phi}$ denotes normalized Φ from 0 to 1. The angle α can be adjusted to enforce fiber continuity at the septum. The modified angle α' is given by:

$$\alpha' = \alpha \cdot (1 - s) + \alpha_{septal} \cdot s. \tag{26}$$

Finally, an additional counterclockwise rotation of vector $\hat{\boldsymbol{e}}_l$ around $\hat{\boldsymbol{e}}_n$ by angle β is applied:

$$\beta = \beta_{endo}(w) \cdot (1 - \tilde{\Phi}) + \beta_{epi}(w) \cdot \tilde{\Phi}, \tag{27}$$

The values of the angles α and β are chosen to match observations from histological studies as in Doste et al. [16]. In particular, the rules for the angle α are derived from Sánchez-Quintana et al. [36], Greenbaum et al. [38], Ho and Nihoyannopoulos [39]:

- left ventricle: $\alpha_{endo}(w = 1) = -60^\circ$; $\alpha_{epi}(w = 1) = 60^\circ$
- right ventricle: $\alpha_{endo}(w = 1) = 90^\circ$; $\alpha_{epi}(w = 1) = -25^\circ$
- outflow tracts: $\alpha_{epi}(w = 0) = 0^\circ$; $\alpha_{endo}(w = 0) = 90^\circ$

and the rules for the angle β are derived from Greenbaum et al. [38], Stephenson et al. [40], Lunkenheimer et al. [41]:

- left ventricle: $\beta_{endo}(w = 1) = -20^\circ$; $\beta_{epi}(w = 1) = 20^\circ$
- right ventricle: $\beta_{endo}(w = 1) = 0^\circ$; $\beta_{epi}(w = 1) = 20^\circ$
- outflow tracts: $\beta_{epi}(w = 0) = 0^\circ$; $\beta_{endo}(w = 0) = 0^\circ$

2.4. Atrial fiber arrangement

Atrial fiber arrangement is commonly generated using manual or semi-automatic approaches based on rule-based or atlas-based methods [42,43]. Recently, a novel LDRBM was proposed to model atrial fiber arrangement with the capacity to reproduce realistic fiber bundles [17]. While the atrial LDRBM is similar to the ventricular LDRBM, the extension of the latter to the atria is not straightforward due to the presence of bundles running in different directions. Therefore, a detailed description of the atrial LDRBM as described in Piersanti et al. [17] is provided here.

The solution of the Laplace problem for the atrial domain dictates the partition of its boundary in several boundaries where Dirichlet boundary conditions should be imposed. Endocardium ($\Gamma_{LAendo}, \Gamma_{RAendo}$), epicardium ($\Gamma_{epi}$), and apex appendage ($\Gamma_{LAA}, \Gamma_{RAA}$) boundaries are defined for both the left atrium (LA) and the right atrium (RA). Additional boundaries are defined for the mitral valve (Γ_{MV}) and the left, right pulmonary veins (Γ_{LPV}, Γ_{RPV}) in LA. Similarly, the boundaries for the inferior and superior caval veins (Γ_{ICV}, Γ_{SCV}), the coronary sinus (Γ_{CS}) and the tricuspid valve (Γ_{TV}) are defined in RA. Γ_{TV} is further subdivided in two parts, where $\Gamma_{TVseptum}$ denotes the part facing the septum and Γ_{TVfree} the part facing the free wall, such that $\Gamma_{TV} = \Gamma_{TVseptum} \cup \Gamma_{TVfree}$. An additional boundary connecting the top upper region of the inferior and superior caval veins (Γ_{TOP}) is defined, which is further divided in two sections, a part lying on the epicardium Γ_{TOPepi} and another one on the endocardium $\Gamma_{TOPendo}$, such that $\Gamma_{TOP} = \Gamma_{TOPepi} \cup \Gamma_{TOPendo}$.

Similarly to the definition of the ventricular fiber arrangement, the transmural distance Φ for the atria is obtained by solving the Laplace problem with Dirichlet boundary conditions applied on Γ_{endo} and Γ_{epi} of both atria. We apply $\Phi = -1$ to Γ_{LAendo} and $\Phi = 1$ to Γ_{RAendo} to allow partitioning the two atria. Furthermore, several intra-atrial distances (Ψ_i), which are used for the bundle selection later on, are obtained by solving the Laplace problem. In particular, Ψ_{AB} is the solution of the Laplace problem with three different boundary values prescribed on the right atrial appendage (Γ_{RAA}), the caval veins (Γ_{SCV}, Γ_{ICV}) and the tricuspid valve (Γ_{TV}) for the RA. In the LA, the boundary values for Ψ_{AB} are defined at the left atrial appendage (Γ_{LAA}), the pulmonary veins (Γ_{LPV}, Γ_{RPV}) and the mitral valve (Γ_{MV}). Ψ_v is used to represent the distance between the caval veins for the RA and the distance between the pulmonary veins for LA. Ψ_r stands for the distance between the tricuspid valve (Γ_{TV}) and the caval veins connecting boundary (Γ_{TOP}) for RA, while for LA it denotes the distance between the mitral valve (Γ_{MV}) and the union of the pulmonary veins ($\Gamma_{LPV} \cup \Gamma_{RPV}$). Moreover, Ψ_w denotes the distance between the Γ_{TVfree} and $\Gamma_{TVseptum}$ in the RA. We refer to Table 3 for a description of the prescribed boundary data for the solution of the corresponding Laplace problem. The partition of the atria and the definition of the different intra-atrial distances are depicted in Fig. 3.

The atrial fiber bundles are defined by combining the different intra-atrial directions based on appropriate rules to match histology and DTI observations. At each point in the atrial domain, a unique intra-atrial distance Ψ_i is assigned following the defined bundle rules in both atria. We refer to the supplemental material for the fiber bundle definition algorithms, which have been described in Piersanti et al. [17].

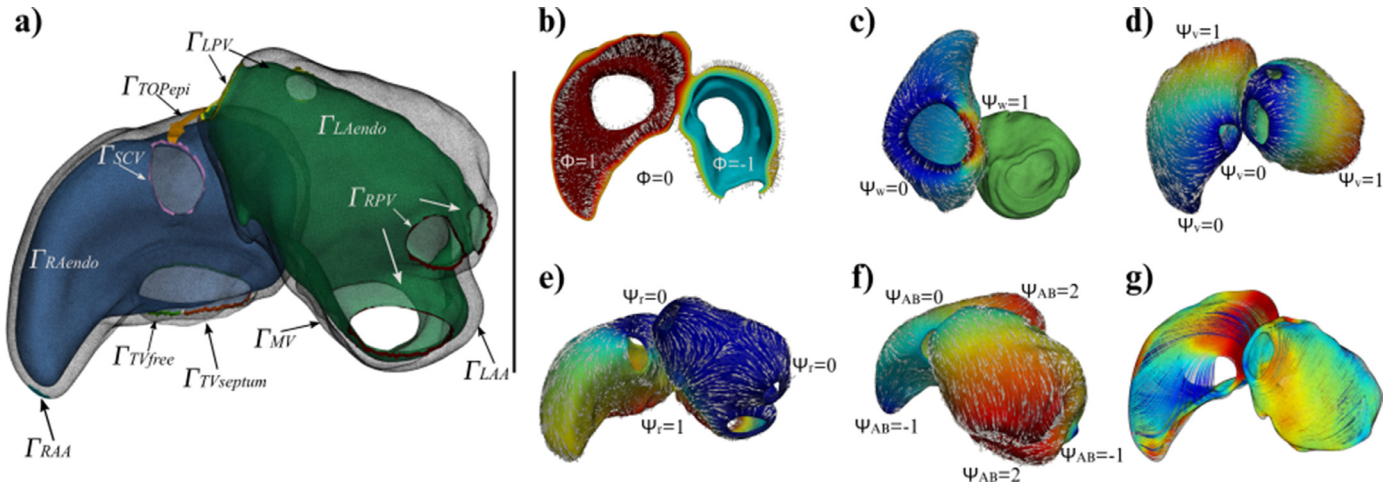

Fig. 3. a) Partition of the atrial geometry boundary. b) Transmural distance (Φ) and its gradient ($\nabla\Phi$). c) Distance (Ψ_w) between $\Gamma_{TV\,free}$ and $\Gamma_{TV septum}$ and its gradient ($\nabla\Psi_w$). d) Distance between the veins (Ψ_v) and its gradient ($\nabla\Psi_v$). e) Valve to veins distance (Ψ_r) and its gradient ($\nabla\Psi_r$). f) Appendage to veins distance ($\Psi_A B$) and its gradient ($\nabla\Psi_A B$). g) Atrial fiber arrangement ($\hat{\boldsymbol{e}}_l$).

Table 3
Boundary conditions for generating atrial fiber orientation.

Type	χ	g_{Da}	Γ_{Da}	g_{Db}	Γ_{Db}
LA	Φ	−1	Γ_{LAendo}	0	Γ_{LAepi}
	Ψ_{ab}	2	Γ_{RPV}	1	Γ_{MV}
		0	Γ_{LPV}	−1	Γ_{LAA}
	Ψ_v	1	Γ_{RPV}	0	Γ_{LPV}
	Ψ_r	1	Γ_{MV}	0	$\Gamma_{LPV} \cup \Gamma_{RPV} \cup \Gamma_{LAA}$
RA	Φ	1	Γ_{RAendo}	0	Γ_{RAepi}
	Ψ_{ab}	2	Γ_{ICV}	1	Γ_{TV}
		0	Γ_{SCV}	−1	Γ_{RAA}
	Ψ_v	1	Γ_{ICV}	0	$\Gamma_{SCV} \cup \Gamma_{RAA}$
	Ψ_r	1	Γ_{TV}	0	Γ_{top}
	Ψ_w	1	Γ_{TV_s}	−1	Γ_{TV_f}

[Da] First Dirichlet condition.
[Db] Second Dirichlet condition.

Table 4
Bundle parameters τ_i to determine atrial fiber orientation.

right atrium	τ_{TV}	τ_{ICV}	τ_{SCV}	τ_{CT+}	τ_{CT-}	τ_{CT+}	τ_{RAS+}	τ_{RAW+}
	0.9	0.85	0.3	−0.55	−0.6	−0.25	−0.1	0.6
left atrium	τ_{MV}	τ_{LPV}	τ_{RPV}					
	0.85	0.85	0.2					

During the fiber bundle assignment, the atrial LDRBM defines a unique normal direction $\nabla\Psi$ by taking the gradient of a specific intra-atrial distance $\nabla\Psi_i$. All the principal anatomical atrial regions are taken into account. Namely, for RA, superior (SCV) and inferior caval veins (ICV), tricuspid valve (TV), right atrium appendage (RAA), septum (RAS), inter-caval bundle (IB), crista terminalis (CT), isthmus (IST) and atrial lateral wall (RAW). For LA, left (LPV) and right (RPV) pulmonary veins, mitral valve (MV), left atrium appendage (LAA), septum (LAS), septum wall (LSW), atrial lateral wall (LAW) and roof (LAR). Moreover, the dimension of the bundles is specified by defining the parameters τ_i. Namely, for the RA we have τ_{TV}, τ_{IB}, τ_{ICV}, τ_{SCV}, τ_{CT^+}, τ_{CT^-}, τ_{RAW} and τ_{RAS} referring to TV, IB, ICV, SCV, and upper, lower limit of CT bundles, respectively; for LA, we have τ_{MV}, τ_{LPV} and τ_{RPV} referring to MV, LPV and RPV bundles respectively. The bundle parameters τ_i used for atrial fiber generation in this work are summarized in Table 4.

Finally, the local coordinate system ($\hat{\boldsymbol{e}}_l, \hat{\boldsymbol{e}}_n, \hat{\boldsymbol{e}}_t$) is defined in the same way as for the ventricles. Since transmural variation is not prescribed in the fiber bundles, the three unit directions correspond to the final longitudinal, sheet normal and transverse directions. The atrial fiber bundle definition rules are based on the following histo-anatomical and DT-MRI fiber data observations [12,44–49]:

- Circular fiber arrangement is defined in LPV, RPV, SCV, ICV, TV, MV, encircling both appendages (RAA and LAA)
- CT fibers run longitudinally from the base of SCV to ICV
- RA bundles are almost vertically oriented and RAS bundles are parallel to CT
- IST fibers follow the same direction as the fibers of TV
- LAS fibers are parallel to the nearby RAS fibers
- LAR and LAW fibers descend perpendicularly to MV, while LSW fibers transition smoothly to LAS and LAA

3. Results

We generated fiber arrangements for ventricular and atrial models using the FPM implementation of the LDRBM (FPM-LDRBM) and we validated the obtained results with fiber arrangements that were computed using FEM. We considered four different models of ventricular and atrial anatomy obtained from a publicly available dataset of four-chamber healthy heart models [50,51]. In all cases, we used a penalty coefficient $\eta = 1$ for the solution of the Laplace problems in FPM-LDRBM. All simulations were performed on a laptop with Intel® Core™ i9-12900H CPU and 32 GB RAM.

3.1. Model preprocessing

The four-chamber models considered in this study were made available as pre-partitioned tetrahedral meshes. The predefined partitions included ventricular and atrial myocardium, aorta and pulmonary artery walls, vein inlets, etc. For the purpose of this study the ventricular and atrial sub-meshes were extracted separately. From the extraction process, rough edges at the connecting borders occurred.

To obtain tetrahedral meshes with smooth surfaces, we extracted the triangular surface meshes of the geometries and processed them with MeshLab [52]. We applied the Laplacian smoothing filter available in MeshLab with mean angle displacement of 0.5° for 20 iterations. The smoothed surfaces were then tetrahedralized using the Iso2Mesh toolkit [53] to obtain tetrahedral meshes of the ventricles and atria with smooth boundaries. Boundaries for the application of the Dirichlet boundary conditions were

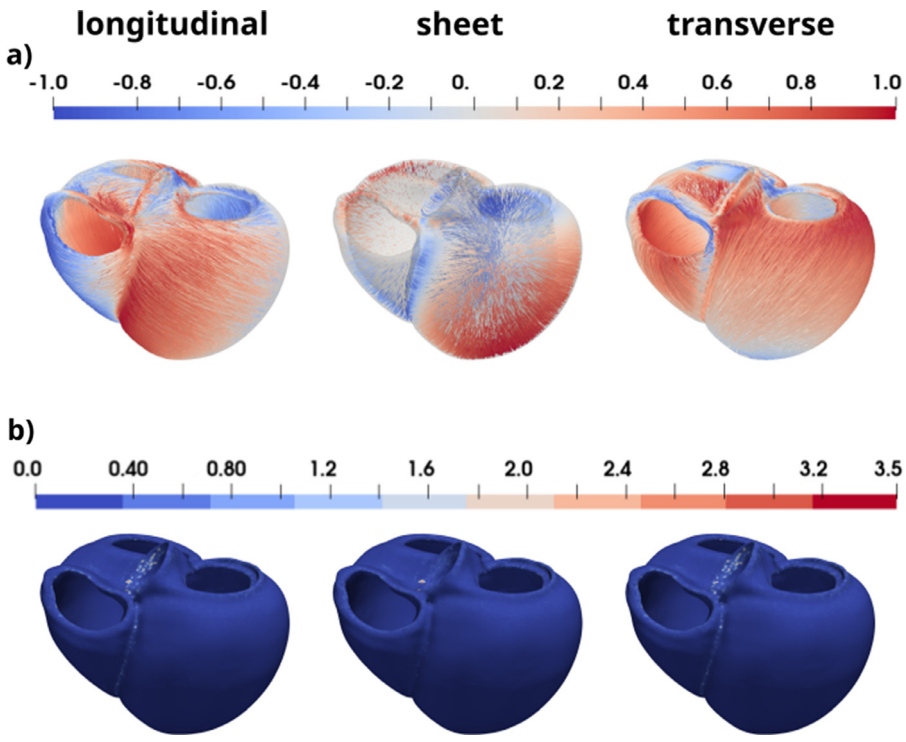

Fig. 4. Ventricular fiber arrangement generated by FPM-LDRBM. a) X-component of fiber direction vectors, b) angle between ventricular fiber arrangements generated by FPM-LDRBM and FEM-LDRBM.

manually selected for the newly meshed tetrahedral meshes using Paraview [54]. We refer to Table 1 for tetrahedral mesh-related information.

Next, a polyhedral partition of the ventricular and atrial geometries was generated to be used in the FPM-LDRBM. To allow for a point-to-point comparison of FPM-LDRBM and FEM-LDRBM, we generated dual polyhedral meshes of the original tetrahedral ones using a dual polyhedral mesh generation algorithm [55,56].

3.2. Ventricular fiber arrangement validation

Ventricular fiber arrangement was generated with the FPM-LDRBM and was compared with the fiber arrangement generated by FEM-LDRBM for the four models. The comparison was performed by calculating the angle (θ) formed between the fiber vectors corresponding to the two solutions for all three directions (longitudinal, sheet normal, transverse). A 0° angle corresponded to a perfect match between the two solutions.

Fiber vectors of the two solutions were found in close agreement at all directions. The mean angle at longitudinal direction (θ_l) was found in the range $\theta_l = [0.019^\circ, 0.024^\circ]$. Similarly, the mean angles at sheet normal (θ_s) and transverse (θ_t) directions were found in the range $\theta_s = [0.018^\circ, 0.030^\circ]$ and $\theta_t = [0.012^\circ, 0.016^\circ]$, respectively. We refer to Table 5 for a detailed report on ventricular $\theta_l, \theta_s, \theta_t$ for the four models. A color map of the $\theta_l, \theta_s, \theta_t$, as well as the ventricular fiber arrangement at the three directions for model M1 is shown in Fig. 4. A colormap for all the four ventricular models is provided in the Supplementary material. Finally, Table 7 summarizes the required computational time for the FPM-LDRBM and FEM-LDRBM solutions for each model.

Table 5
Angle (in degrees) between FPM-LDRBM and FEM-LDRBM ventricular fiber direction vectors.

Angle	Model	Mean	Min	Max
θ_l	M1	0.019175	0	3.124371
	M2	0.021179	0	3.075247
	M3	0.02364	0	1.82537
	M4	0.024088	0	1.982917
θ_s	M1	0.018926	0	3.125336
	M2	0.025917	0	3.01845
	M3	0.029618	0	1.825447
	M4	0.030146	0	1.982459
θ_t	M1	0.016384	0	2.843894
	M2	0.011733	0	2.307241
	M3	0.014368	0	0.872051
	M4	0.014345	0	1.103488

Table 6
Angle (in degrees) between FPM-LDRBM and FEM-LDRBM atrial fiber direction vectors.

Angle	Model	Mean	Min	Max
θ_l	M1	0.027199	0	3.132266
	M2	0.024881	0	3.102739
	M3	0.032493	0	3.132507
	M4	0.026971	0	3.140188
θ_s	M1	0.026346	0	3.088409
	M2	0.023373	0	3.123649
	M3	0.023362	0	3.098048
	M4	0.022651	0	3.008890
θ_t	M1	0.030390	0	3.137769
	M2	0.027577	0	3.090940
	M3	0.035785	0	3.123759
	M4	0.030149	0	3.131334

3.3. Atrial fiber arrangement validation

Similarly, atrial fiber vectors of the FPM-LDRBM and FEM-LDRBM solutions were found in close agreement at all directions. Mean (θ_l) was found in the range $\theta_l = [0.025^\circ, 0.032^\circ]$, mean θ_s and mean θ_t were found in the range $\theta_s = [0.023^\circ, 0.026^\circ]$ and $\theta_t = [0.028^\circ, 0.036^\circ]$, respectively. We refer to Table 6 for a detailed report on atrial $\theta_l, \theta_s, \theta_t$ for the four models. The color map of the $\theta_l, \theta_s, \theta_t$ and the arrangement of the atrial fibers at the three

Table 7
Computational time for FPM-LDRBM and FEM-LDRBM ventricular fiber arrangements. $t_{assembly}$: assembly of the algebraic system matrix, $t_{\nabla\Phi}$: computation of transmural direction, t_s: computation of septum fiber continuity function, t_w: computation of intraventricular interpolation function, $t_{\nabla\Psi}$: computation of apicobasal direction, t_{fibers}: computation of fiber arrangement .

Method	Model	$t_{assembly}$ (s)	$t_{\nabla\Phi}$ (s)	t_s (s)	t_w (s)	$t_{\nabla\Psi}$ (s)	t_{fibers} (s)
FPM	M1	1.93	0.93	0.27	4.38	12.32	0.02
LDRBM	M2	1.74	0.93	0.28	3.55	10.60	0.02
	M3	1.60	0.80	0.26	3.23	10.29	0.02
	M4	1.52	0.72	0.19	3.24	9.48	0.01
FEM	M1	1.37	0.82	0.23	3.71	10.90	0.02
LDRBM	M2	1.27	0.78	0.24	2.98	9.22	0.02
	M3	1.15	0.71	0.22	2.86	8.65	0.01
	M4	1.10	0.64	0.17	2.79	8.24	0.01

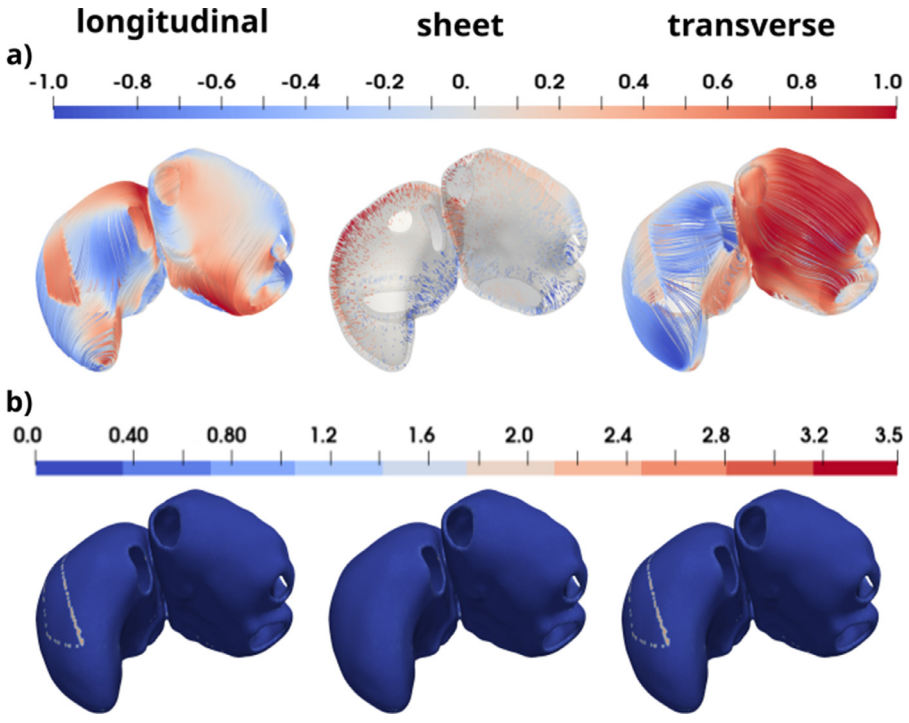

Fig. 5. Atrial fiber arrangement generated by FPM-LDRBM. a) X-component of fiber direction vectors, b) angle between atrial fiber arrangements generated by FPM-LDRBM and FEM-LDRBM.

Table 8
Computational time for FPM-LDRBM and FEM-LDRBM atrial fiber arrangements. $t_{assembly}$: assembly of the algebraic system matrix, $t_{\nabla\Phi}$: computation of transmural direction, $t_{\nabla\Psi_{AB}}$: computation of appendage to valves direction, $t_{\nabla\Psi_v}$: computation of caval to pulmonary veins direction, $t_{\nabla\Psi_r}$: computation of tricuspid valve to caval veins direction, $t_{\nabla\Psi_w}$: computation of free tricuspid valve to septum direction, t_{fibers}: computation of fiber arrangement .

Method	Model	$t_{assembly}$ (s)	$t_{\nabla\Phi}$ (s)	$t_{\nabla\Psi_{AB}}$ (s)	$t_{\nabla\Psi_v}$ (s)	$t_{\nabla\Psi_r}$ (s)	$t_{\nabla\Psi_w}$ (s)	t_{fibers} (s)
FPM	M1	0.80	0.37	2.46	2.49	2.46	1.30	0.02
LDRBM	M2	0.88	0.39	2.61	2.74	2.73	1.50	0.03
	M3	0.84	0.44	2.85	3.16	2.67	1.48	0.03
	M4	0.79	0.36	2.61	2.82	2.59	1.31	0.02
FEM	M1	0.56	0.32	2.10	2.20	2.05	1.11	0.02
LDRBM	M2	0.61	0.33	2.23	2.36	2.31	1.28	0.03
	M3	0.61	0.37	2.46	2.72	2.32	1.25	0.03
	M4	0.56	0.31	2.23	2.35	2.27	1.17	0.02

directions for model M1 is given in Fig. 5. A colormap for all the four atrial models is also provided in the Supplementary material. Finally, Table 8 summarizes the required computational time for the FPM-LDRBM and FEM-LDRBM solutions for each model.

4. Discussion

Currently existing LDRBM have been implemented using FEM to determine myocardial fiber arrangement [16,17]. Therefore, even if meshless methods are used for the simulation of cardiac electrophysiology [27], the generation of a mesh is inevitable. The purpose of this work was to provide a meshless solution to the Laplace–Dirichlet problem so that fibers can be determined without requiring a mesh. According to our knowledge, this is the first time that a meshless method is applied to solve this problem.

We implemented a solver for the Laplace–Dirichlet problem using the FPM method [30] to determine both ventricular and atrial fiber orientations. We demonstrated the capacity of FPM to solve

the Laplace–Dirichlet problem for fiber generation with similar accuracy to FEM. As shown in Figs. 4 and 5, the difference between the fiber arrangement computed by FPM and FEM was negligible. The angle between the FPM and FEM fiber vectors was almost 0° for both ventricular and atrial fiber orientations in all directions (i.e. longitudinal, transverse and sheet normal). Maximum angle difference was about 3° and occurred at nodes located at sharp features where large gradients are expected to appear. However, the maximum angle difference was small enough to allow considering the solution obtained by FPM similar to that by FEM. In terms of computational efficiency, FPM was found to be up to 20% less efficient than FEM. This computational overhead was mainly due to the application of the numerical flux continuity during the assembly of the algebraic system matrix. In the solution of the algebraic system, the computational overhead was minimum since the matrix bandwidth in FPM is restricted by using compact support domains, see Table 7 and Table 8.

We used the same angle rules for angles α and β for ventricular fiber generation in all four considered models. Similarly, the same bundle parameters τ_i were used in all four models for atrial fiber determination. As our objective was to compare the obtained solutions by FPM and FEM, the choice of α, β and τ_i was not particularly relevant. Modifying the values of α and β allows adjusting ventricular fiber orientation and controlling for septum continuity. Similarly, modification of τ_i allows controlling the size of the atrial fiber bundles. By modifying these parameters, the LDRBM-determined fibers can be adjusted to fit patient-specific data.

The proposed LDRBM method allowed to determine the fiber arrangement for complete cardiac models (ventricular and atrial fiber arrangements) without requiring the construction of a mesh as in FEM-based methods. This can be of high interest, as it enables to set fully meshless cardiac models for the investigation of cardiac electrophysiology and function. In future work, we plan to investigate the capacity of LDRBM for determination of patient-specific fiber orientation using electrical and mechanical data to estimate local modifications to the angles α, β and τ_i that could allow personalizing LDRBM. Such personalized LDRBM would contribute to precision medicine in clinical cardiology.

Declaration of Competing Interest

The authors declare that they have no known competing financial interests or personal relationships that could have appeared to influence the work reported in this paper.

Acknowledgments

The authors declare that the research was conducted in the absence of any commercial or financial relationships that could be construed as a potential conflict of interest. This work was supported by Ministerio de Ciencia e Innovación (Spain) through project PID2019-105674RB-I00, by the European Research Council under grant agreement ERC-StG 638284, and by European Social Fund (EU) and Aragón Government through project LMP94_21 and BSICoS group T39_20R. Computations were performed by the ICTS NANBIOSIS (HPC Unit at University of Zaragoza).

Supplementary material

Supplementary material associated with this article can be found, in the online version, at 10.1016/j.cmpb.2022.107164

References

[1] C.-Y. Chung, H. Bien, E. Entcheva, The role of cardiac tissue alignment in modulating electrical function, J. Cardiovasc. Electrophysiol. 18 (12) (2007) 1323–1329.

[2] R.C.P. Kerckhoffs, J.H. Omens, A.D. McCulloch, A single strain-based growth law predicts concentric and eccentric cardiac growth during pressure and volume overload, Mech. Res. Commun. 42 (2012) 40–50.

[3] A.P. Voorhees, H.-C. Han, A model to determine the effect of collagen fiber alignment on heart function post myocardial infarction, Theor. Biol. Med. Model. 11 (1) (2014) 1–19.

[4] D.F. Scollan, A. Holmes, J. Zhang, R.L. Winslow, Reconstruction of cardiac ventricular geometry and fiber orientation using magnetic resonance imaging, Ann. Biomed. Eng. 28 (8) (2000) 934–944.

[5] C.T. Stoeck, A. Kalinowska, C. Von Deuster, J. Harmer, R.W. Chan, M. Niemann, R. Manka, D. Atkinson, D.E. Sosnovik, C. Mekkaoui, et al., Dual-phase cardiac diffusion tensor imaging with strain correction, PLoS One 9 (9) (2014) e107159.

[6] A. Gonzalez-Tendero, C. Zhang, V. Balicevic, R. Cárdenes, S. Loncaric, C. Butakoff, B. Paun, A. Bonnin, P. Garcia-Cañadilla, E. Muñoz Moreno, et al., Whole heart detailed and quantitative anatomy, myofibre structure and vasculature from X-ray phase-contrast synchrotron radiation-based micro computed tomography, Eur. Heart Journal-Cardiovascular Imaging 18 (7) (2017) 732–741.

[7] W.-N. Lee, M. Pernot, M. Couade, E. Messas, P. Bruneval, A. Bel, A.A. Hagege, M. Fink, M. Tanter, Mapping myocardial fiber orientation using echocardiography-based shear wave imaging, IEEE Trans. Med. Imaging 31 (3) (2011) 554–562.

[8] S. Nielles-Vallespin, C. Mekkaoui, P. Gatehouse, T.G. Reese, J. Keegan, P.F. Ferreira, S. Collins, P. Speier, T. Feiweier, R. de Silva, M.P. Jackowski, D.J. Pennell, D.E. Sosnovik, D. Firmin, In vivo diffusion tensor MRI of the human heart: reproducibility of breath-hold and navigator-based approaches, Magn. Reson. Med. 70 (2) (2013) 454–465.

[9] C. Nguyen, Z. Fan, Y. Xie, J. Pang, P. Speier, X. Bi, J. Kobashigawa, D. Li, In vivo diffusion-tensor MRI of the human heart on a 3 Tesla clinical scanner: an optimized second order (M2) motion compensated diffusion-preparation approach, Magn. Reson. Med. 76 (5) (2016) 1354–1363.

[10] O. Dössel, M.W. Krueger, F.M. Weber, M. Wilhelms, G. Seemann, Computational modeling of the human atrial anatomy and electrophysiology, Med. Biol. Eng. Comput. 50 (8) (2012) 773–799.

[11] J. Zhao, B.J. Hansen, Y. Wang, T.A. Csepe, L.V. Sul, A. Tang, Y. Yuan, N. Li, A. Bratasz, K.A. Powell, et al., Three-dimensional integrated functional, structural, and computational mapping to define the structural æfingerprintsg of heart-specific atrial fibrillation drivers in human heart ex vivo, J. Am. Heart Assoc. 6 (8) (2017) e005922.

[12] F. Pashakhanloo, D.A. Herzka, H. Ashikaga, S. Mori, N. Gai, D.A. Bluemke, N.A. Trayanova, E.R. McVeigh, Myofiber architecture of the human atria as revealed by submillimeter diffusion tensor imaging, Circulation 9 (4) (2016) e004133.

[13] R. Beyar, S. Sideman, A computer study of the left ventricular performance based on fiber structure, sarcomere dynamics, and transmural electrical propagation velocity, Circ. Res. 55 (3) (1984) 358–375.

[14] J.D. Bayer, J. Beaumont, A. Krol, Laplace–Dirichlet energy field specification for deformable models. an FEM approach to active contour fitting, Ann. Biomed. Eng. 33 (9) (2005) 1175–1186.

[15] J.D. Bayer, R.C. Blake, G. Plank, N.A. Trayanova, A novel rule-based algorithm for assigning myocardial fiber orientation to computational heart models, Ann. Biomed. Eng. 40 (10) (2012) 2243–2254.

[16] R. Doste, D. Soto-Iglesias, G. Bernardino, A. Alcaine, R. Sebastian, S. Giffard-Roisin, M. Sermesant, A. Berruezo, D. Sanchez-Quintana, O. Camara, A rule-based method to model myocardial fiber orientation in cardiac biventricular geometries with outflow tracts, Int. J. Numer. Method Biomed. Eng. 35 (4) (2019) e3185.

[17] R. Piersanti, P.C. Africa, M. Fedele, C. Vergara, L. Dedè, A.F. Corno, A. Quarteroni, Modeling cardiac muscle fibers in ventricular and atrial electrophysiology simulations, Comput. Methods Appl. Mech. Eng. 373 (2021) 113468.

[18] L. Tung, A bi-Domain Model for Describing Ischemic Myocardial DC Potentials, Massachusetts Institute of Technology, 1978 Ph.D. thesis.

[19] J.P. Keener, J. Sneyd, Mathematical Physiology: Systems Physiology. II, Springer, 2009.

[20] S.N. Atluri, S. Shen, The basis of meshless domain discretization: the meshless local Petrov–Galerkin (MLPG) method, Adv. Comput. Math. 23 (1–2) (2005) 73–93.

[21] Y. Gu, Meshfree methods and their comparisons, Int. J. Comput. Methods 2 (04) (2005) 477–515.

[22] H. Zhang, H. Ye, W. Huang, A meshfree method for simulating myocardial electrical activity, Comput. Math. Methods Med. (2012) 1–16.

[23] M. Arroyo, M. Ortiz, Local maximum-entropy approximation schemes: a seamless bridge between finite elements and meshfree methods, Int. J. Numer. Methods Eng. 65 (13) (2006) 2167–2202.

[24] K.A. Mountris, G.C. Bourantas, D. Millán, G.R. Joldes, K. Miller, E. Pueyo, A. Wittek, Cell-based maximum entropy approximants for three-dimensional domains: application in large strain elastodynamics using the meshless total lagrangian explicit dynamics method, Int. J. Numer. Methods Eng. 121 (3) (2020) 477–491.

[25] K.A. Mountris, E. Pueyo, The radial point interpolation mixed collocation (RPIMC) method for the solution of the reaction-diffusion equation in cardiac electrophysiology, in: International Conference on Computational & Experimental Engineering and Sciences, Springer, 2021, pp. 39–44.

[26] K.A. Mountris, E. Pueyo, Next-generation in silico cardiac electrophysiology through immersed grid meshfree modeling: application to simulation of myocardial infarction, in: 2020 Computing in Cardiology, IEEE, 2020, pp. 1–4.

[27] K.A. Mountris, E. Pueyo, Cardiac electrophysiology meshfree modeling through the mixed collocation method, arXiv preprint arXiv:2110.06671(2021).
[28] T. Yang, L. Dong, S.N. Atluri, An elementarily simple Galerkin meshless method: the fragile points method (FPM) using point stiffness matrices, for 2d elasticity problems in complex domains, arXiv preprint arXiv:1909.04149(2019).
[29] Y. Guan, L. Dong, S.N. Atluri, A new meshless fragile points method (FPM) with minimum unknowns at each point, for flexoelectric analysis under two theories with crack propagation, i: theory and implementation, J. Mech. Mater. Struct. 16 (2) (2021) 159–195.
[30] Y. Guan, S.N. Atluri, Meshless fragile points methods based on Petrov—Galerkin weak-forms for transient heat conduction problems in complex anisotropic nonhomogeneous media, Int. J. Numer. Methods Eng. 122 (16) (2021) 4055–4092.
[31] K. Wang, B. Shen, M. Li, L. Dong, S.N. Atluri, The fragile points method, with an interface damage model, to simulate damage and fracture of u-notched structures, arXiv preprint arXiv:2108.12737(2021).
[32] K.A. Mountris, L. Dong, Y. Guan, S.N. Atluri, E. Pueyo, Meshfree implementation of the cardiac monodomain model through the fragile points method, arXiv preprint arXiv:2111.06975(2021).
[33] T. Liszka, J. Orkisz, The finite difference method at arbitrary irregular grids and its application in applied mechanics, Comput. Struct. 11 (1–2) (1980) 83–95.
[34] D.N. Arnold, F. Brezzi, B. Cockburn, L.D. Marini, Unified analysis of discontinuous Galerkin methods for elliptic problems, SIAM J. Numer. Anal. 39 (5) (2002) 1749–1779.
[35] L. Dong, T. Yang, K. Wang, S.N. Atluri, A new fragile points method (FPM) in computational mechanics, based on the concepts of point stiffnesses and numerical flux corrections, Eng. Anal. Bound. Elem. 107 (2019) 124–133.
[36] D. Sánchez-Quintana, M. Doblado-Calatrava, J.A. Cabrera, Y. Macías, F. Saremi, Anatomical basis for the cardiac interventional electrophysiologist, Biomed. Res. Int. (2015) 1–24.
[37] P. Agger, S. Lakshminrusimha, C. Laustsen, S. Gugino, J.R. Frandsen, M. Smerup, R.H. Anderson, V. Hjortdal, R.H. Steinhorn, The myocardial architecture changes in persistent pulmonary hypertension of the newborn in an ovine animal model, Pediatr. Res. 79 (4) (2016) 565–574.
[38] R.A. Greenbaum, S.Y. Ho, D.G. Gibson, A.E. Becker, R.H. Anderson, Left ventricular fibre architecture in man, Heart 45 (3) (1981) 248–263.
[39] S.Y. Ho, P. Nihoyannopoulos, Anatomy, echocardiography, and normal right ventricular dimensions, Heart 92 (suppl 1) (2006) i2–i13.
[40] R.S. Stephenson, P. Agger, P.P. Lunkenheimer, J. Zhao, M. Smerup, P. Niederer, R.H. Anderson, J.C. Jarvis, The functional architecture of skeletal compared to cardiac musculature: myocyte orientation, lamellar unit morphology, and the helical ventricular myocardial band, Clin. Anat. 29 (3) (2016) 316–332.
[41] P.P. Lunkenheimer, P. Niederer, D. Sanchez-Quintana, M. Murillo, M. Smerup, Models of ventricular structure and function reviewed for clinical cardiologists, J. Cardiovasc. Transl. Res. 6 (2) (2013) 176–186.
[42] C. Tobón, C.A. Ruiz-Villa, E. Heidenreich, L. Romero, F. Hornero, J. Saiz, A three--dimensional human atrial model with fiber orientation. electrograms and arrhythmic activation patterns relationship, PLoS One 8 (2) (2013) e50883.
[43] S. Rocher, A. López, A. Ferrer, L. Martínez, D. Sánchez, J. Saiz, A highly-detailed 3D model of the human atria, in: World Congress on Medical Physics and Biomedical Engineering 2018, Springer, 2019, pp. 649–653.
[44] D. Sánchez-Quintana, J.R. López-Mínguez, Y. Macías, J.A. Cabrera, F. Saremi, Left atrial anatomy relevant to catheter ablation, Cardiol. Res. Pract. (2014) 1–17.
[45] S.Y. Ho, R.H. Anderson, D. Sánchez-Quintana, Atrial structure and fibres: morphologic bases of atrial conduction, Cardiovasc. Res. 54 (2) (2002) 325–336.
[46] S.Y. Ho, D. Sanchez-Quintana, The importance of atrial structure and fibers, Clin. Anat. 22 (1) (2009) 52–63.
[47] S.Y. Ho, J.A. Cabrera, D. Sanchez-Quintana, Left atrial anatomy revisited, Circulation 5 (1) (2012) 220–228.
[48] D. Sánchez-Quintana, G. Pizarro, J.R. López-Mínguez, S.Y. Ho, J.A. Cabrera, Standardized review of atrial anatomy for cardiac electrophysiologists, J. Cardiovasc. Transl. Res. 6 (2) (2013) 124–144.
[49] C.H. Roney, A. Pashaei, M. Meo, R. Dubois, P.M. Boyle, N.A. Trayanova, H. Cochet, S.A. Niederer, E.J. Vigmond, Universal atrial coordinates applied to visualisation, registration and construction of patient specific meshes, Med. Image Anal. 55 (2019) 65–75.
[50] C. Rodero, M. Strocchi, M. Marciniak, S. Longobardi, J. Whitaker, M.D. O'Neill, K. Gillette, C. Augustin, G. Plank, E.J. Vigmond, P. Lamata, S.A. Niederer, Virtual cohort of adult healthy four-chamber heart meshes from CT images, 2021, GP received support from the Austrian Science Fund (FWF) (https://fwf.ac.at/en/); grant number PI2760-B30. PL is supported by BHF [PG/16/75/32383]. SAN is supported by NIH R01-HL152256, ERC PREDICT-HF 453 (864055) and BHF (RG/20/4/34803).
[51] C. Rodero, M. Strocchi, M. Marciniak, S. Longobardi, J. Whitaker, M.D. O'Neill, K. Gillette, C. Augustin, G. Plank, E.J. Vigmond, et al., Linking statistical shape models and simulated function in the healthy adult human heart, PLoS Comput. Biol. 17 (4) (2021) e1008851.
[52] P. Cignoni, M. Callieri, M. Corsini, M. Dellepiane, F. Ganovelli, G. Ranzuglia, MeshLab: an open-source mesh processing tool, in: V. Scarano, R. De Chiara, U. Erra (Eds.), Eurographics Italian Chapter Conference, The Eurographics Association, 2008, pp. 129–136.
[53] Q. Fang, D.A. Boas, Tetrahedral mesh generation from volumetric binary and grayscale images, in: 2009 IEEE International Symposium on Biomedical Imaging: From Nano to Macro, IEEE, 2009, pp. 1142–1145.
[54] J. Ahrens, B. Geveci, C. Law, Paraview: an end-user tool for large data visualization, Vis. Handb. 717 (8) (2005) 1–17.
[55] R.V. Garimella, J. Kim, M. Berndt, Polyhedral mesh generation and optimization for non-manifold domains, in: Proceedings of the 22nd International Meshing Roundtable, Springer, 2014, pp. 313–330.
[56] J. Kim, An efficient approach for solving mesh optimization problems using Newton's method, Math. Probl. Eng. (2014) 1–9.